Photographic, magnetic, and interferometric measurements of current sheet canting in a pulsed electromagnetic accelerator

T.E. Markusic*and E.Y. Choueiri†
Electric Propulsion and Plasma Dynamics Laboratory (EPPDyL)
Mechanical and Aerospace Engineering Department
Princeton University, Princeton, New Jersey 08544

AIAA 2001-3896‡

July 11, 2001

Abstract

The propagation speed and canting angle of current sheets in a pulsed electromagnetic accelerator were measured using three different techniques: high-speed photography, magnetic field probes, and laser interferometry. Current sheet canting may have adverse effects on accelerator performance. The goal of the present work is to provide a database of canting angles under a variety of experimental conditions. Eight different propellants (hydrogen, deuterium, helium, neon, argon, krypton, xenon, and methane) were tested in a rectangular-geometry accelerator, at pressures ranging from 50-400 mTorr. The photographic, magnetic, and interferometric diagnostics were used to infer the spatial configuration of the current sheet by measuring the its optical emission, current density, and electron density, respectively. The three techniques gave qualitative agreement; the magnetic and interferometric measurements gave general quantitative agreement as well. The canting angle was found to depend on the atomic mass of the propellant; lighter atoms were observed to yield less canting (the measured angles ranged from approximately 20^o for deuterium to 70^o for xenon). Hydrogen, deuterium, and methane were found to exhibit the peculiar, and possibly beneficial, property of having reduced current sheet canting at higher pressures.

1 Introduction

Pulsed electromagnetic accelerators are devices which use intense bursts of electrical current (10^4-10^6 A) to create high speed (10^3-10^5 m/s) jets of plasma. They find application as plasma sources in many basic plasma science experiments[1] as well as in a specific genre of electric space propulsion device called the pulsed plasma thruster (PPT)[2].

PPTs have the potential of fulfilling the attitude control requirements on a satellite at greatly reduced mass and cost. They are also being considered for constellation maintenance for missions such as interferometric imaging of the Earth from space or deep space from an Earth orbit. The benefits of PPTs are their very small impulse bits ($\sim 10^{-4}$ N-s) for precise control of satellite motion, reliability, and high specific impulse. Two classifications of PPTs exist, corresponding to the form of propellant used: gas-fed (GFPPT) or ablative propellant (APPT). The

*Current address: NASA MSFC, Huntsville, AL 35802. Member AIAA.

†Chief Scientist at EPPDyL. Assistant Professor, Applied Physics Group. Senior Member AIAA.

‡Presented at the 37^{th} AIAA Joint Propulsion Conference, Salt Lake City, Utah, July 8-11, 2001.

gas-fed variety has the advantages of a "clean" exhaust plume and high specific impulse. The ablative version of the PPT uses a solid propellant, such as Teflon, to provide further advantages such as compactness and overall ease of system integration; however, plume contamination and lower specific impulse may limit the application of APPTs for some missions.

From about 1960 to 1968 PPT research focused on the gas-fed varient. The GFPPT was envisioned as a potential "primary" propulsion system, wherein the GFPPT would process large amounts of power ($>$100 kW), and provide enough average thrust ($>$1 N) to perform large Δv maneuvers, such as interplanetary missions. By the late sixties it was realized that a steady-flow electromagnetic accelerator, the MPD thruster[3], was better suited for this type of mission. A "secondary" propulsion niche, i.e., small Δv attitude control maneuvers, still existed for the GFPPT. However, at about the same time, the ablative variety of PPT was gaining favor, mainly due to its mechanical simplicity. The GFPPT requires the storage of gaseous propellant under high pressure and a fast-acting valve to meter puffs of propellant into the discharge chamber. Further, the propellant feed system in the GFPPT is required to operate in a leak-free manner for many ($> 10^6$) shots. A qualified system capable of performing this demanding task was not available at the time and, hence, only APPTs were flown[4].

This state-of-affairs remained until the mid-90's, when the negative issues related to propellant feeding in the GFPPT were ameliorated by the availability of flight-qualified valves and the development of high-speed solid-state electrical switching technology. The former development addressed the reliability issue, while the latter showed promise for substantially increasing the propellant utilization efficiency. These technologies were implemented in the thrusters of Ziemer *et al.*[5].

With the renewed interest in GFPPTs it is fitting and natural that there is a revitalized interest in understanding the physical principles which underlie PPT operation, in order to improve their performance. Careful review of the work of earlier researchers[6] shows that our understanding of the acceleration mechanism in PPTs is deficient in several areas. Our current research aims to clear up one such area of ambiguity – current sheet canting.

2 Review of the problem

The phenomenon of current sheet canting is the departure of the current sheet from perpendicular attachment to the electrodes to a skew, or tipped attachment. This effect is best illustrated by an example. Figure 1 shows a series of photographs acquired in our previous study[7]. The figure shows the evolution of a discharge near the breech of a rectangular-geometry pulsed electromagnetic accelerator; outlines of the electrodes (the cathode is the bottom electrode) have been added for clarity. Ideally, we would like the current sheet to initiate at the breech, perpendicular to the electrodes, and remains so as it propagates axially. In the figure, as expected, the current sheet is seen to initiate at the breech; however, as time progresses, the current sheet is seen to severely tilt, or cant, as it propagates. It is important to develop an understanding of why the current sheet tilts as it does because it may have adverse implications on PPT performance; canting may create off-axis components of thrust, which constitute a profile loss.

We are, by no means, the first group to observe current sheet canting. The literature from the early GFPPT researchers (see, for example, [8]-[16]) indicates that the phenomenon was ubiquitous – occurring in a variety of different electrode geometries and experimental conditions. However, detailed treatment of the subject is limited, with most references to the phenomenon being qualitative in nature.

The photographs shown in figure 1 were some of the earliest observations[7] in an experiment we designed to understand the basic macroscopic stability of current sheets under a variety of experimental conditions. The observed severity of the current sheet canting warranted further investigation; the present study, which we call the Current Sheet Canting Experiment (CSCX), aims to accurately quantify the degree of tilting under a variety of experimental con-

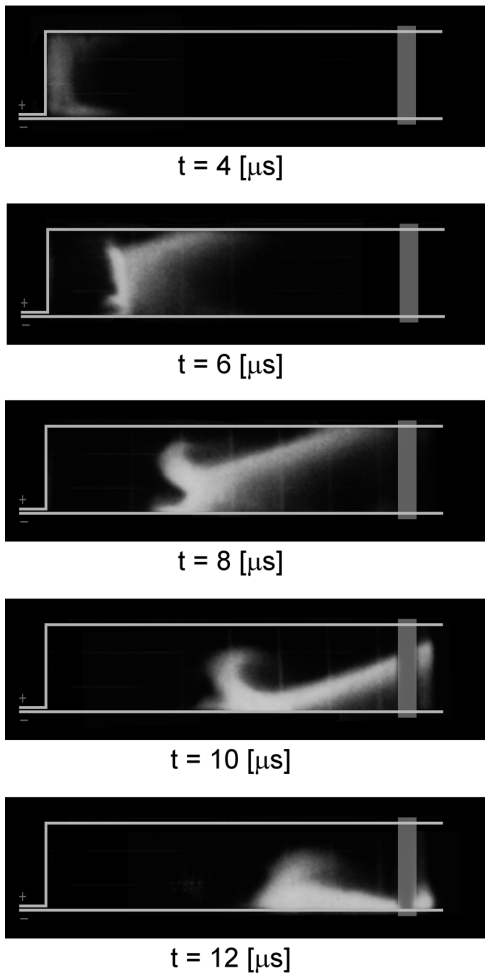

Figure 1: Series of photographs showing the evolution of the discharge near the breech[7](p=100 mTorr (Argon), V=5 kV).

ditions (e.g., using different propellants and pressures), develop theoretical models to explain the phenomenon and, ultimately, provide prescriptions for how to reduce the effect and, in turn, enable the design of higher performance pulsed plasma thrusters. The present work summarizes our experimental findings. Its main purpose is to provide a database of canting angles for a variety of different experimental conditions. By using this data in ongoing and future theoretical work, we hope to identify the physical mechanisms which drive current sheet canting. The two sections which follow give details about the

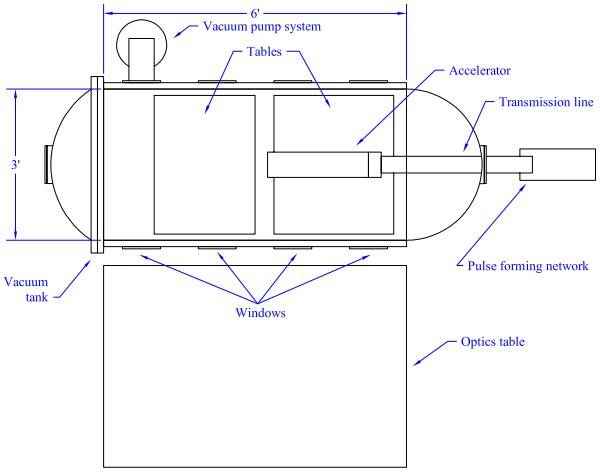

Figure 2: Top-view schematic of the general experimental layout.

experimental apparatus and diagnostics. Next, the experimental results are presented. The last section summarizes and compares the various results, and discusses trends which are evident in the data.

3 Apparatus

An experimental pulsed electromagnetic accelerator has been constructed. The accelerator was not designed to be a practical thruster but, rather, a device in which current sheets could be generated and easily observed. The details of this accelerator and the associated experimental facilities are described in the sections which follow.

3.1 General experimental layout

The basic components of the CSCX experimental apparatus are the accelerator, pulse forming network, and vacuum facility. The layout of these components is illustrated in Fig. 2.

The tables inside the vacuum chamber support the accelerator and provide mounting surfaces for optics and diagnostic probes. A 4’$\times$ 6’ optics table, positioned next to the tank, was used to lay out optical diagnostics. Glass windows on the sides of the vacuum chamber provided optical access to the acceler-

ator discharge.

The overriding design rationale was to create an experimental configuration which provides convenient access to optical and probe diagnostics. Secondarily, it was desired that the configuration would be amenable to analytic modelling (e.g., one-dimensional electromagnetic fields, constant current, etc.).

3.2 CSCX Accelerator

The CSCX Accelerator is a parallel plate pulsed plasma accelerator with glass sidewalls (a schematic illustration with relevant dimensions is shown in Fig. 3). The dimensions of the discharge chamber were chosen to be similar to those found to "work" by earlier researchers (see, for example, Eckbreth[17]). The electrodes are made of copper and the sidewalls are made of Pyrex. The sidewalls reduce the region accessible to the discharge to 10 cm (width), whereas the electrodes themselves are 15 cm wide. The motivation for using Pyrex sidewalls is several-fold: first, they provide an excellent optical view of the discharge, second, they isolate the current sheet to a well defined spatial region, third, they isolate the discharge from electric field singularities which are associated with the sharp edges of the electrodes, and last, they isolate the discharge from the rapidly fringing magnetic field at the edges of the electrodes. The two latter benefits tend to make the discharge environment more conducive to the formation of spatially uniform current sheets.

Propellant loading was accomplished using the ambient fill technique. After the vacuum tank was pumped down to its base pressure (1×10^{-5} Torr), the entire tank was brought to the desired operating pressure with the chosen propellant (hydrogen, deuterium, helium, neon, argon, krypton, xenon, and methane were used in the present study). This resulted in a uniform gas distribution within the accelerator prior to discharge initiation.

The accelerator is powered by a ten-stage pulse forming network (PFN). The values of the electrical components at each stage were chosen to give a nearly flat current profile with a pulse width that

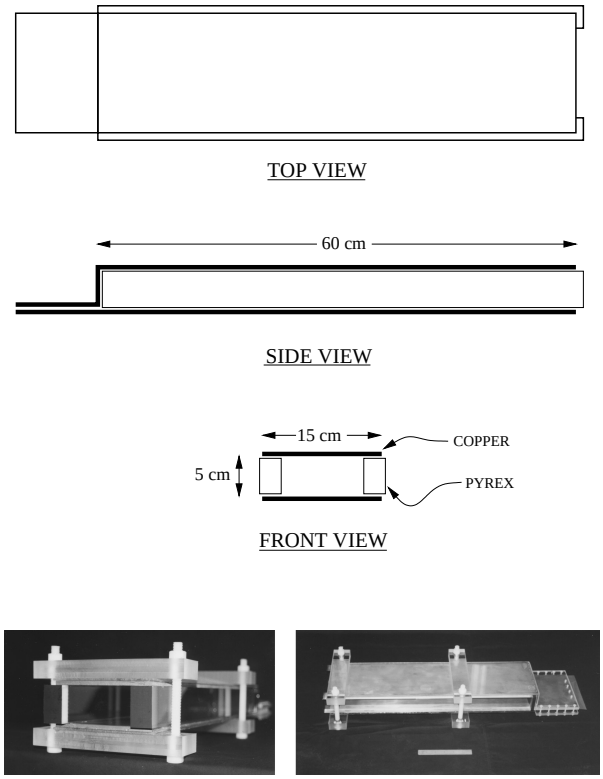

Figure 3: Schematic and photographs of the CSCX accelerator.

corresponds to the time it takes the current sheet to traverse the length of the accelerator. Each stage is composed of a 10 μF capacitor in series with a 100 nH inductor. The maximum bank voltage was 10 kV, yielding a total discharge energy of 5 kJ. The PFN was switched into the accelerator using an ignitron. The peak current was approximately 80 kA, with an initial rise rate on the order of 10^{11} A/s. The duration of each pulse was about 25 μs, which was followed by one cycle of damped ringing. A typical current trace is shown in Fig. 4. In the present study, all experiments were conducted with 9 kV initial bank voltage.

In general, the apparatus performed very well; current sheets were generated in the expected manner (i.e., formation at the breech and propagation to the exit) and the experiments were very repeatable. Photographs taken of different discharges (with the same initial conditions and same camera time delay) were

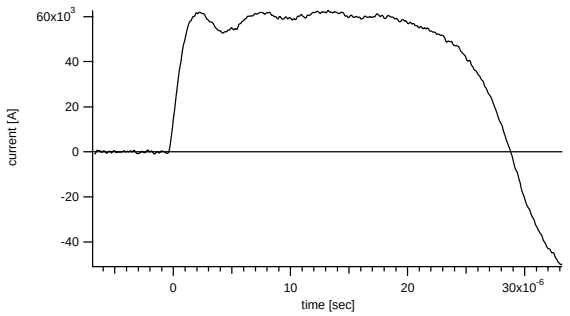

Figure 4: Typical current waveform (propellant: helium (p=75 mTorr) , voltage: 9 kV).

practically indistinguishable.

3.3 Vacuum facility

The vacuum facility used in this experiment is described in detail by Jahn [18]. The vacuum vessel is a 1 m diameter, 2 m long cylindrical tank made entirely of Plexiglass (which has been shown to eliminate the electromagnetic interactions sometimes found in metallic vessels), with glass optical access windows. Gases are introduced into the tank using a regulated feed-through. The tank uses a diffusion pump with a freon-cooled trap to achieve a base pressure of 1×10^{-5} Torr. Sub-milliTorr pressures are measured with a CVC cold cathode gauge. All pressures above one mTorr are monitored using a MKS Baratron vacuum gauge.

4 Diagnostics

This section gives detailed descriptions of the diagnostics which were applied to obtain measurements of the current sheet propagation speed and canting angle in the CSCX accelerator.

4.1 High-speed photography

The camera used in this study, a Hadland Photonics Imacon 792LC, is capable of taking pictures at a rate of up to 20 MHz and provides up to sixteen images printed on Polaroid film. In the experiments presented here, the framing rate was set to 500 kHz;

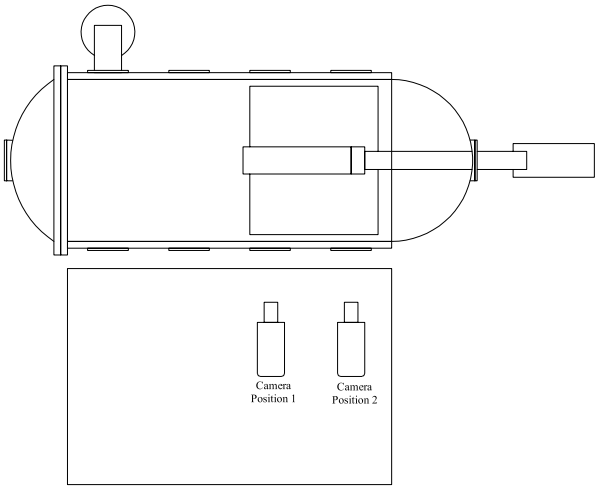

Figure 5: Schematic of high speed photography experimental layout.

the exposure time for each image was 400 ns. This camera was useful for creating movies which show how the discharge evolves spatially during the entire pulse.

The layout of the photography experiment is shown in figure 5. The camera was placed at one of two positions. Position 1 was used to photograph the breech section of the accelerator; position 2 was used to photograph the mid-section. In order to more easily visualize the spatial position of the current sheets and to estimate the size and orientation of current sheet features, a black screen with white gridding (1 cm spacing) was placed on the outside of one side of the accelerator. The propagation speed of the current sheet was estimated by comparing successive frames in a single shot (with known inter-frame time delay.) The canting angle was estimated graphically, using the photographs, by drawing two lines, one parallel to the cathode and one parallel to the luminous front, and measuring the angle between them.

4.2 Magnetic field probes

Magnetic field probes were used to determine the current sheet canting angle by monitoring the response of two probes at different spatial locations and inferring the spatial configuration of the current

sheet through a time-of-flight analysis.

The magnetic field probes used in this study were magnetic induction coils, commonly referred to as b-dot probes. These probes are simply linear coils of wire that generate an emf proportional to the time variation of the magnetic flux through the coil. So, experimentally, we determine the local magnetic field by evaluating the expression

$$B(t') = \int_0^{t'} c(\omega) V dt \ , \qquad (1)$$

where V is the measured probe voltage and $c(\omega)$ is a (frequency dependent) parameter determined through calibration.

The particular probes used in our study were acquired from an earlier experiment[19] (the details of the probe construction are shown in Fig. 6.) The probes were calibrated by placing them in the uniform-field region of a Helmholtz coil; pulses of known current and frequency were driven through the Helmholtz coil and the probe response was recorded. The probes' frequency response is expected to be linear in $\mathrm{d}B/\mathrm{dt}$ [i.e., $c(\omega) = c$, a constant] through $\omega \leq 100$ MHz, due to the probes' low inductance; however, we verified the linearity only up to approximately 2 MHz, which was sufficient for our purposes. No analog integration was used; instead, the probe voltage was measured directly and integrated numerically to determine $B(t')$.

Two probes were used in two different configurations, as illustrated in Fig. 6. In configuration 1, the probes were placed inside the accelerator in the same horizontal plane (separated by approximately 2.5 cm), and separated axially by approximately Δx_1 = 20 cm. During a discharge the two probe responses were simultaneously monitored. By dividing the known axial probe separation by the difference in the arrival time of the current sheet to each probe (Δt_1), the average current sheet propagation speed ($v = \Delta x_1/\Delta t_1$) was determined, In configuration 2 the probes were placed at the same axial position, but vertically displaced by approximately Δy = 3 cm. By measuring the time delay between the arrival times of the current sheet to each probe (Δt_2), and multiplying by the previously determined value of v, we can determine the axial displacement of the current channel ($\Delta x = v\Delta t_2$) and, hence, the current sheet canting angle ($\tan\theta = \Delta x/\Delta y$) relative to the electrode normal.

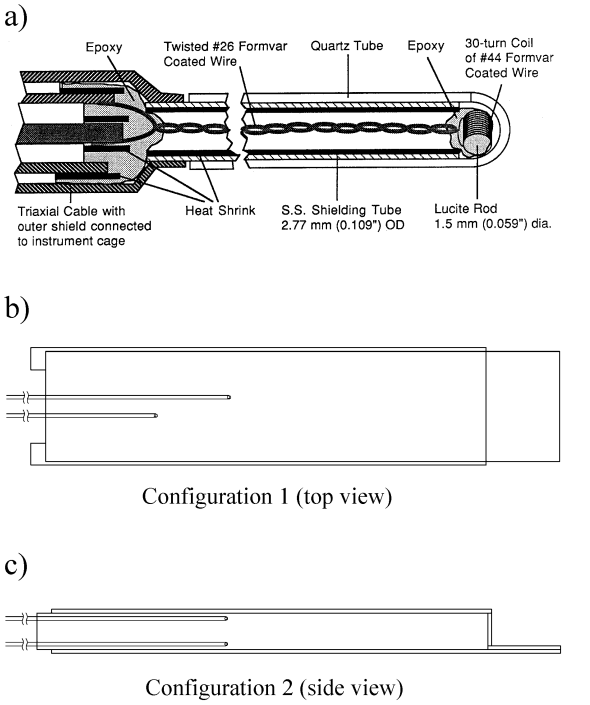

Figure 6: Magnetic field probe schematics: a) probe construction details[19], b) probe placement for speed determination, c) probe placement for canting angle determination.

4.3 Laser interferometry

A two-chord heterodyne laser interferometer with electronic quadrature phase detection was constructed; the system is very similar to the single-chord system implemented by Spanjers *et al.*[20] in APPT research. A schematic of the experiment layout is shown in Fig. 7. In a manner similar to the previously described magnetic field diagnostic, the interferometer was used to determine the current sheet speed and canting angle by monitoring the phase variations of two laser beams at different spatial locations within the accelerator and inferring the spatial configuration of the current sheet through a time-of-

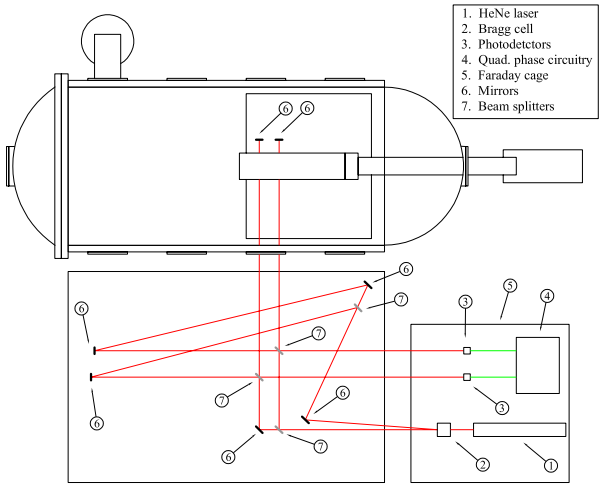

Figure 7: Schematic of laser interferometry layout.

flight analysis.

The system consists of two interferometers in the Mach-Zehnder configuration. This type of interferometer detects phase differences between the "scene" and "reference" beams. When these two beams are recombined at the detector, any phase mismatches between the beams causes amplitude variations in the detector output due to constructive or destructive interference. In our experiment, phase differences between the two paths arise when the current sheet plasma passes through the scene beam; the plasma index of refraction (n) is different than that of free space ($n_\circ$) and, hence, the scene beam optical path changes as the current sheet passes by. By measuring the phase change of the scene beam we can determine the change in optical path length and, in turn, the effective index of refraction of the plasma. Finally, through a suitable theoretical model of the interaction of the laser beam's electromagnetic wave with the plasma, the electron density of the plasma can be determined.

The simplest model of the plasma-EM wave interaction assumes a weak magnetic field and isotropic plasma, in which case it can be shown that[21]

$$n = \sqrt{1 - \frac{\omega_p^2}{\omega^2}} \ , \tag{2}$$

where, ω_p is the plasma frequency and ω is the laser radiation frequency. Additionally, if $\omega_p \ll \omega$, the number density of electrons in terms of the measured phase shift is approximated by

$$n_e = \frac{2cn_c}{\omega l}\Delta\phi \ , \tag{3}$$

where, c is the speed of light in vacuum, l is the physical length of the plasma through which the beam propagates, and n_c is the so-called cutoff density, above which the beam is reflected out of the plasma:

$$n_c \equiv \omega^2 m_e \epsilon_\circ / e^2 \ . \tag{4}$$

In our particular implementation, equation 3 reduces to

$$n_e = 2.78 \times 10^{15} \ \Delta\phi \ [\mathrm{cm}^{-3}] \ . \tag{5}$$

Two problems arise in the interpretation of data obtained with a conventional Mach-Zehnder interferometer: amplitude variations in the detected signal which arise from attenuation or refractive bending in the plasma must be distinguished from phase variations, and in general it is not possible to determine the direction of the phase change (i.e., positive phase changes cannot be distinguished from negative ones.) These problems can be eliminated by using a heterodyne light source and quadrature phase detection. In a heterodyne system, either the scene or reference beam is phase modulated at the source; when the beams are recombined at the detector the amplitude of the detected signal will oscillate at the modulation frequency; the task of detecting the phase changes due to the plasma becomes measuring the phase of the oscillation at the detector relative to the driving modulation at the source. The technology for this type of measurement, which is essentially one of homodyne detection, has been well developed by the radio reception community. Drawing on this knowledge, we have developed a two-channel quadrature phase detector. Each channel uses two double balanced mixers to produce output signals proportional to the sine and cosine of the phase and, hence, unambiguously determines the quadrant of the phase angle. A schematic of one channel of the phase detection circuitry is shown in Fig. 8.

The specific components used in the interferometer were as follows. The light source was a Coherent

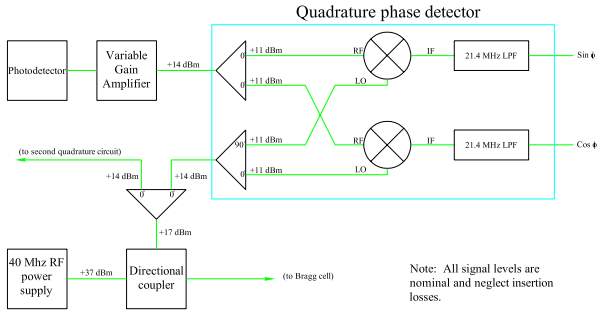

Figure 8: Schematic of one channel of the interferometer quadrature phase detection circuitry.

model 31-2108 17 mW HeNe laser. The beam splitting into the scene and reference beam, along with modulation of the reference beam, was accomplished using an IntraAction model AOM-405 acousto-optic cell driven by a 40 Mhz, 5 W RF power source. Two Thor Labs model PDA155 photo detectors were used. These amplified (1×10^4 V/A) Si detectors have a 50 Mhz bandwidth. It was found that, because of the large amount of electromagnetic noise created by the firing of the accelerator, all electronics, including the laser, had to be housed in a Faraday cage. Standard optical component (aluminized mirrors, dielectric beam splitters, and anti-reflection windows) were used to steer the beams.

The current sheet propagation speed and and canting angle were determined in a completely analogous manner to that used in the analysis of the magnetic field waveforms. The response from two horizontally separated beams (approximately 10 cm axial separation) were used to determine the propagation speed (the orientation of the optics for this experiment is illustrated in Fig. 7.) The beams were retro-reflected back through the plasma to give twice the phase shift of a single pass. For canting angle determination, two beams at the same axial location but vertically separated by about 3.5 cm were used.

No direct calibration of the instrument was carried out (i.e., the response of the system to a known change in optical path length was not attempted.) It is difficult to conceive of how such a procedure could be accomplished. The phase variations measured by the detector due to room vibrations and atmospheric fluctuations alone reduce the useful time scale of the device to experiments which last less than 100 μsec. It is unclear how one would introduce an object of known optical path length into the scene beam on such a short time scale. We have, however, based simply on signal to noise considerations, estimated the minimal resolvable variation in electron density in our device to be on the order of 1×10^{14} cm^{-3}. The spatial resolution, which was limited by the laser beam diameter, was about 3 mm.

5 Experimental Results

Three diagnostics (high-speed photography, magnetic field probes, and laser interferometry) were used to estimate the current sheet propagation speed and canting angle. The results of these measurements are presented below. In each section, a single, representative data set will be graphically illustrated followed by a complete tabulation of the resulting data base and associated errors.

5.1 High-speed photography

Photographs were taken of the mid-section of the accelerator, with the camera in position 2 (see Fig. 5.) Seven different propellants were used at either 2 or 3 pressure levels (75, 200, and 400 mTorr.) Higher atomic mass propellants (e.g. xenon) were not photographed at 400 mTorr because the current pulse was not of sufficient duration to drive the discharge into the viewing region for higher mass loadings.

The goal of the high-speed photography experiment was to get a rough idea of the current sheet propagation speed and canting angle. The diagnostic is not well suited for precise measurements because interpretation of the photographs relies on the assumption that the luminosity patterns correspond to the spatial location of the current. This assumption may not be valid if the luminous regions are caused by other phenomena, such as shock waves.

Figure 9 shows examples of the photographs obtained in the study. For clarity, the position of the electrodes (anode on top) have been added using image processing software. Also, the gridded back-

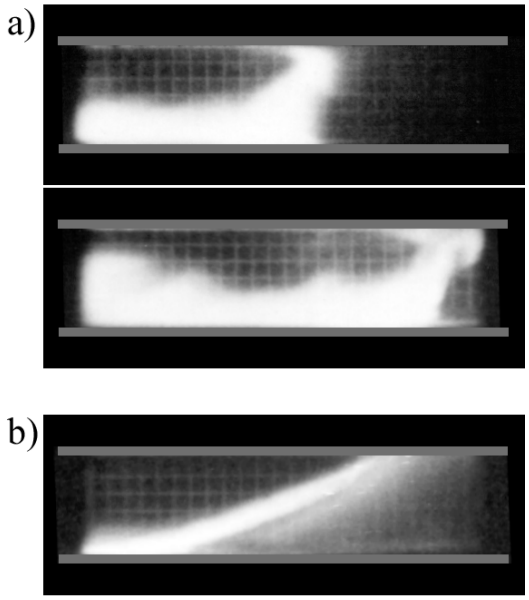

Figure 9: High-speed photographs of current sheets in the midsection of the CSCX accelerator: a) Example of photographs used in the determination of propagation speed (helium (400 mTorr), Δt = 2 μsec between frames), b) Example of a photograph used to determine canting angle (xenon (75 mTorr)).

Table 1: Current sheet propagation speed and canting angle from photographic data.

species	pressure [mTorr]	speed [cm/μsec]	canting angle [degrees]
hydrogen	75 ± 2	-	27
hydrogen	200 ± 2	-	22
hydrogen	400 ± 2	5.5	16
deuterium	75 ± 2	-	25
deuterium	200 ± 2	6	26
deuterium	400 ± 2	4.5	24
helium	75 ± 2	6.0	38
helium	200 ± 2	5.0	40
helium	400 ± 2	4.5	41
neon	75 ± 2	5.5	62
neon	200 ± 2	4.0	60
neon	400 ± 2	4.0	59
argon	75 ± 2	4.5	63
argon	200 ± 2	3.0	61
krypton	75 ± 2	4.5	67
krypton	200 ± 2	2.5	65
xenon	75 ± 2	2.5	68
xenon	200 ± 2	-	64

ground outside of the accelerator is visible (the grid spacing was 1 cm.) In the pictures the current sheet is moving from left to right. The right-most visible feature, which spans the entire gap between the electrodes, is assumed to be the current sheet. Also, a luminous cloud is seen to trail behind the current sheet; we assume that this is not part of the current conduction zone but, rather, gas that has been heated by the current sheet. Figure 9a shows two images from a helium discharge, taken 2 μsec apart. By measuring the change in spatial position of the sheet between the two frames, the propagation speed was estimated. Figure 9b shows a single frame from a xenon discharge. By measuring the slope of the luminous front, the canting angle was estimated. Table 1 summarizes the measurements obtained from all of the photographs.

Each entry in table 1 was distilled from two photographs. In some cases the images were difficult to interpret (for example, the high speed of the hydrogen current sheets caused the images to be blurred); those cases are indicated by dashes in the table. No meaningful error analysis can be carried out on the given values because of the small number of samples as well as the inherent subjectivity in the interpretation of the luminosity patterns.

In any event, some qualitative trends can be gleaned from the results. First, the higher atomic weight propellant cases had slower moving current sheets, which is what one would expect from mass loading considerations. Second, it is apparent that the higher atomic mass propellants had a higher degree of current sheet canting – with xenon having almost 40^o more of a tilt than hydrogen. Hydrogen

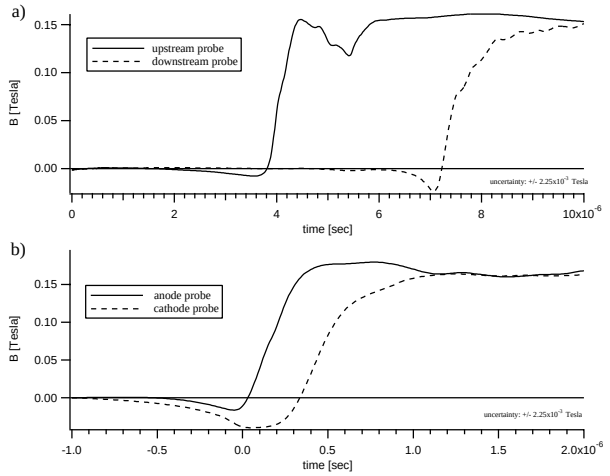

Figure 10: Magnetic field measurements using b-dot probes for time-of-flight canting angle analysis, in a) configuration 1 and b) configuration 2 (Hydrogen (75 mTorr).)

at high pressure exhibited the lowest canting angle.

5.2 Magnetic field probes

In order to obtain a more accurate measurement of the current sheet speed and canting angle, two magnetic field probes were introduced into the accelerator channel as illustrated in Fig. 6. The same propellants and pressures used in the photographic study were tested.

Figure 10 shows a typical set of data with hydrogen as a propellant. In Fig. 10a the b-dot probes were aligned according to configuration 1 (see Fig. 6.) In this orientation, the probes were axially separated by 21 cm. We see that, as the current sheet approaches the probe, the magnetic field in front of the sheet is gradually detected; then, as the probe enters the current channel, the magnetic field quickly reverses direction. When the current sheet has passed the probe, the magnetic field reaches its peak value and remains fairly constant until the current reverses. Data such as that shown in Fig. 10a can be used to estimate (using the time-of-flight technique) the current sheet propagation speed by measuring the time delay between a common feature on each waveform (e.g., the point of field reversal.) Similarly, in Fig. 10b, the b-dot probes were aligned in configuration 2. In this orientation, the probes were vertically spaced 3 cm. By measuring the time delay between the arrival time of the current sheet to each probe and, knowing the propagation speed of the current sheet, the canting angle can be estimated. Table 2 summarizes all of the speed and canting angle measurements using the magnetic field probes and time-of-flight analysis. Each entry in table 2 represents the average of two experimental measurements. The error associated with having only two samples is large, and is reflected in the large error bars in the tabulated values.

Table 2: Current sheet propagation speed and canting angle from magnetic probe data. Indicated error is for a 90% confidence interval.

species	pressure [mTorr]	speed [cm/μsec]	canting angle [degrees]
hydrogen	75 ± 2	6.5 ± 1.2	39 ± 8
hydrogen	200 ± 2	5.6 ± 1.0	44 ± 7
hydrogen	400 ± 2	4.6 ± 0.8	20 ± 8
deuterium	75 ± 2	6.8 ± 0.9	52 ± 7
deuterium	200 ± 2	5.5 ± 0.9	46 ± 6
deuterium	400 ± 2	3.9 ± 0.8	27 ± 6
helium	75 ± 2	6.9 ± 1.3	49 ± 9
helium	200 ± 2	5.3 ± 0.9	54 ± 6
helium	400 ± 2	4.9 ± 0.8	49 ± 5
neon	75 ± 2	5.2 ± 0.8	55 ± 6
neon	200 ± 2	4.2 ± 0.7	58 ± 5
neon	400 ± 2	3.0 ± 0.7	56 ± 5
argon	75 ± 2	5.0 ± 0.9	62 ± 5
argon	200 ± 2	3.2 ± 0.7	57 ± 4
krypton	75 ± 2	4.4 ± 1.4	71 ± 8
krypton	200 ± 2	2.3 ± 0.7	63 ± 4
xenon	75 ± 2	3.6 ± 0.6	67 ± 4
xenon	200 ± 2	1.8 ± 0.6	56 ± 4

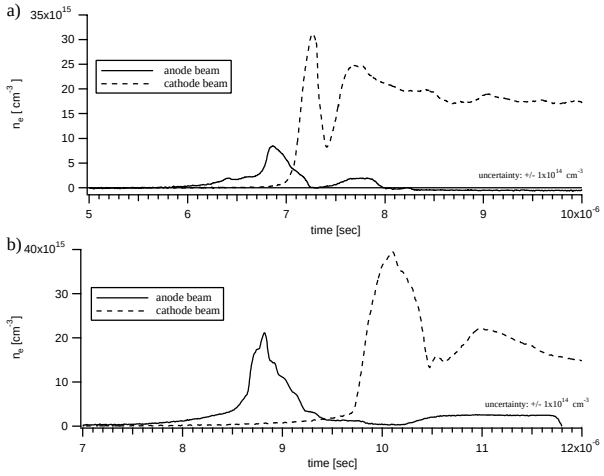

Figure 11: Electron density measurements using laser interferometer for time-of-flight canting angle analysis(configuration 2): a) helium (75 mTorr), b) argon (75 mTorr).

The trends found in the photographic data are also evident in the magnetic field data: the speed of the current sheet decreases with increased mass loading and, in general, the current sheet canting is more severe for the higher atomic mass propellants. Comparison of the numerical values in both tables shows general agreement with one major exception: the magnetic field data shows that the canting angle of the hydrogen and deuterium current sheets is much larger than inspection of the photographs would indicate. However, the markedly lower (compared to all other propellant-pressure combinations) canting angle in high pressure hydrogen and deuterium is observed in both the photographic and magnetic data.

Table 3: Current sheet propagation speed and canting angle measurements from laser interferometer. Indicated error is for a 90% confidence interval.

species	pressure [mTorr]	speed [cm/μsec]	canting angle [degrees]
hydrogen	75 ± 2	7.7 ± 0.5	48 ± 4
hydrogen	200 ± 2	5.9 ± 0.2	47 ± 5
hydrogen	400 ± 2	4.4 ± 0.2	31 ± 4
deuterium	75 ± 2	6.9 ± 0.3	49 ± 5
deuterium	200 ± 2	4.9 ± 0.2	41 ± 3
deuterium	400 ± 2	3.6 ± 0.1	20 ± 4
helium	75 ± 2	6.7 ± 0.2	40 ± 5
helium	200 ± 2	5.5 ± 0.1	50 ± 4
helium	400 ± 2	4.4 ± 0.3	52 ± 3
neon	75 ± 2	5.3 ± 0.2	50 ± 2
neon	200 ± 2	4.0 ± 0.2	57 ± 4
neon	400 ± 2	2.9 ± 0.1	60 ± 4
argon	75 ± 2	4.1 ± 0.4	56 ± 4
argon	200 ± 2	2.9 ± 0.2	59 ± 3
krypton	75 ± 2	3.9 ± 0.1	65 ± 3
krypton	200 ± 2	2.4 ± 0.1	64 ± 3
xenon	75 ± 2	3.5 ± 0.1	67 ± 3
xenon	200 ± 2	1.9 ± 0.1	59 ± 5
methane	50 ± 2	5.6 ± 0.4	48 ± 3
methane	75 ± 2	5.2 ± 0.5	57 ± 4
methane	200 ± 2	2.7 ± 0.3	29 ± 5

5.3 Laser interferometry

The final diagnostic implemented to measure the current sheet speed and canting angle was a two chord laser interferometer (see Fig. 7.) In addition to the propellant-pressure combinations described in the preceding sections, methane was tested at 50, 75, and 200 mTorr. The interferometry experiment was carried out in a manner completely analogous to the magnetic field measurement experiment: two axially separated laser beams (configuration 1) were used to measure the current sheet speed (see Fig. 7) and two vertically separated beams (configuration 2) were used to measure the canting angle.

Figure 11 shows examples of electron density measurements acquired with the interferometer aligned in configuration 2 (4 cm vertical beam separation.) In both plots we see, in agreement with our previous observations, that the current sheet arrives first at the anode beam location. Also, it is clear that the cathode current sheet attachment in helium, while

lagging behind the anode attachment, arrives earlier than in the case of argon, indicating less canting. Another readily apparent feature, common to both gases, is the large disparity in electron density near the cathode as compared to near the anode. Also, the cathode traces indicate that a layer of plasma persists along the cathode long after the current sheet has passed by.

Table 3 summarizes the speed and canting angle measurements from the interferometric diagnostic and time-of-flight analysis. Each entry is the result of five experimental measurements and, hence, has a smaller error bar than in the magnetic field experiment.

Comparison of the data in tables 2 and 3 shows, within the bounds of the given error bars, that all of the major trends discussed in the interpretation of the magnetic field data are also borne out by the interferometric data. Also, methane (which is largely composed of hydrogen) exhibits the same peculiar tendency as hydrogen and deuterium – reduced canting at higher pressures.

6 Discussion and Conclusions

The propagation speed and canting angle of current sheets in a pulsed electromagnetic accelerator were measured using three different techniques: high-speed photography, magnetic field probes, and laser interferometry. Eight different propellants (hydrogen, deuterium, helium, neon, argon, krypton, xenon, and methane) were tested in a rectangular-geometry accelerator, at pressures ranging from 50-400 mTorr. The canting angle was found to be dependent on the atomic mass of the propellant; lighter atoms were observed to yield less canting(the measured angles ranged from approximately 20^o for deuterium to approximately 70^o for xenon). Hydrogen, deuterium, and methane were found to exhibit the peculiar, and possibly beneficial, property of having reduced current sheet canting at higher pressures.

The magnetic field and interferometry diagnostics gave, in general, quantitative agreement. The analysis of the photographic data, however, gave significantly different estimates of the canting angle for the lower atomic mass propellants. Evidently, some of the luminous regions in the photographs are not zones of current flow but originate from other processes.

Although the goal of the study represented in this paper is to provide an experimental database of canting angles for use in ongoing and future theoretical studies, we wish to make a few preliminary comments on some of the features apparent in the data.

Referring to the electron density data in Fig. 11, we see that the electron density on the anode side is much lower than that on the cathode side (note: both beams are about 1 cm away from each electrode – well outside the electrode Debye sheath regions.) This density imbalance may suggest that the effect of canting is to force the plasma entrained by the current sheet into the cathode where it stagnates and is then left behind. This picture is supported by the cathode laser beam electron density traces, that show a significant plasma density which persists after the current sheet has passed. Also, the photographs in Fig. 9 show a long luminous layer of plasma behind the current sheet. These data indicate that, in addition to causing an off-axis component of thrust, current sheet canting may undermine the effective sweeping up of propellant as the current sheet propagates. Indeed, canted current sheets may act like real ”snowplows” – never accumulating but, rather, throwing their load to the side as they pass by. We emphasize that this is only one of many possible interpretations of the data; other explanations, such as electrode erosion or the liberation of adsorbed gas may in fact be the cause of the measured anode-cathode electron density disparity.

The data in all of the experiments indicate that current sheet canting is reduced when lighter atomic mass propellants are used. Furthermore hydrogen and deuterium showed markedly lower canting at higher pressures. However, hydrogen is not an ideal PPT propellant, due to the difficulty of handling cryogenic propellants on a spacecraft. To practically exploit the benefits of low current sheet canting which results from the use of hydrogen at high pressure, we sought alternative propellants which contain a significant amount of hydrogen in their molecular

structure. Alkanes, with their $C_N H_{2N+2}$ structure, seemed like a natural choice. Methane was tested as part of the interferometric study and was found to have the same reduced canting behavior (at higher pressures) as hydrogen. Further tests are needed on longer-chain hydrocarbons. If butane, for example, is found to exhibit similar behavior, it will be an appealing GFPPT propellant on two levels. In addition to the aforementioned canting benefits, butane can be stored as a liquid under relatively low pressure at room temperature; therefore, a butane propellant system will have a much smaller specific volume (smaller fuel tank and feed system) than a high pressure gas system.

References

[1] J. Marshal. Performance of a hydromagnetic plasma gun. *The Physics of Fluids*, 3(1):134–135, January-February 1960.

[2] R.G. Jahn. *Physics of Electric Propulsion*. McGraw-Hill Book Company, 1968.

[3] R.G. Jahn K.E. Clark. Quasi-steady plasma acceleration. In *AIAA* 7^{th} *Electric Propulsion Conference*, Williamsburg, Virginia, March 3-5 1969. AIAA 69-267.

[4] P.J. Turchi and R.L. Burton. Pulsed plasma thruster. *J. Propulsion and Power*, 14(5):716–735, Sept.-Oct. 1998.

[5] J.K. Ziemer, E.A. Cubbin, E.Y. Choueiri, and D. Birx. Performance characterization of a high efficiency gas-fed pulsed plasma thruster. In 33^{rd} *Joint Propulsion Conference*, Seattle, Washington, July 6-9 1997. AIAA 97-2925.

[6] J.K. Ziemer. A review of gas-fed pulsed plasma thruster research over the last half-century. Princeton University, 2000.

[7] T.E. Markusic and E.Y. Choueiri. Visualization of current sheet canting in a pulsed plasma accelerator. In 26^{th} *International Electric Propulsion Conference*, Kitakyushu, Japan, October 17-21 1999. IEPC 99-206.

[8] J.C. Keck. Current distribution in a magnetic annular shock tube. *The Physics of Fluids*, 5:630–632, 1962.

[9] F.J. Fishman and H. Petschek. Flow model for large radius-ratio magnetic annular shock-tube operation. *The Physics of Fluids*, 5:632–633, 1962.

[10] R.B. Johansson. Current sheet tilt in a radial magnetic shock tube. *The Physics of Fluids*, 8(5):866–871, 1964.

[11] W.H. Bostick. Hall currents and vortices in the coaxial plasma accelerator. *The Physics of Fluids*, 6(11), 1963.

[12] L.C. Burkhardt and R.H. Lovberg. Current sheet in a coaxial plasma gun. *The Physics of Fluids*, 5(3):341–347, March 1962.

[13] L. Liebing. Motion and structure of a plasma produced in a rail spark gap. *The Physics of Fluids*, 6:1035–1036, 1962.

[14] J.R. MacLelland, A.S.V. MacKenzie, and J. Irving. Schlieren photography of rail-tube plasmas. *Research Notes*, pages 1613–1615, April 1966.

[15] R.H. Lovberg. The measurement of plasma density in a rail accelerator by means of schlieren photography. *IEEE Transactions on Nuclear Science*, pages 187–198, January 1964.

[16] R.L. Burton. *Structure of the Current Sheet in a Pinch Discharge*. PhD thesis, Princeton University, 1966.

[17] A.C. Eckbreth. *Current Pattern and Gas Flow Stabilization in Pulsed Plasma Accelerators*. PhD thesis, Princeton University, 1968.

[18] R.G. Jahn and K.E. Clark. A large dielecteic vacuum facility. *AIAA Journal*, 1966.

[19] W.A. Hoskins. Asymmetric discharge patterns in the mpd thruster. Master's thesis, Princeton University, 1990.

[20] G. Spanjers. Propellant inenefficiencies in pulsed plasma thrusters. In 6^{th} *Aerospace Sciences Meeting*, New York, New York, January 22-24 1998. AIAA 68-85.

[21] I.H. Hutchison. *Principles of Plasma Diagnostics*. Cambridge University Press, 1987.